Radical Voronoï tessellation from random pack of polydisperse spheres: prediction of the cells' size distribution

Dorian Depriester[a,*], Régis Kubler[a]

[a] *Laboratoire MSMP (EA 7350), École Nationale Supérieure d'Arts et Métiers, 2 cours des Arts et Métiers - 13617 Aix-en-Provence (FRANCE)*

Abstract

This paper investigates the relevance of the representation of polycrystalline aggregates using Radical Voronoï (RV) tessellation, computed from Random Close Packs (RCP) of spheres with radius distribution following a lognormal distribution. A continuous relationship between the distribution of sphere radii with that of RV cell volumes is proposed. The stereology problem (deriving the 3D grain size distributions from 2D sections) is also investigated: two statistical methods are proposed, giving analytical continuous relationships between the apparent grain size distribution and the sphere radius distribution. In order to assess the proposed methods, a 3D aggregate has been generated based on a EBSD map of a real polycrystalline microstructure.

Keywords: Polycrystal, Radical Voronoï, Probability Density Function, Stereology

1. Introduction

Polycrystalline materials, such as metals or minerals, are usually composed of numerous individual grains, connected to each other by their grain boundaries. As a result, their thermomechanical properties are strongly influenced by the morphology and the crystalline orientation of each grain. The numerical generation of random geometries, representative of real microstructures, is still challenging because it requires to statistically reproduce the physical properties of the modelled grains in order to model the behaviour of polycrystalline aggregates [1–3].

The Poisson-Voronoï (PV) tessellation [4] has been extensively used over the last decades to numerically generate microstructure similar to real ones [1, 2, 5–9]. Consider a set of n separate points (called seeds) $\{\boldsymbol{p}_1, \boldsymbol{p}_2, ..., \boldsymbol{p}_n\}$ in a given volume Ω. In PV geometry, the i-th cell is defined such that:

$$\mathrm{C}_i = \left\{ \boldsymbol{x} \in \Omega \middle| \|\boldsymbol{x} - \boldsymbol{p}_i\| = \min_{k=1}^{n} \|\boldsymbol{x} - \boldsymbol{p}_k\| \right\} \tag{1}$$

where $\|\cdot\|$ denotes the euclidean distance. The PV tessellation results in a series of convex and non-overlapping cells bounded by planar surfaces. Nevertheless, considering the definition given in (1), size and shape of each

*Corresponding author
Email address: dorian.depriester@ensam.eu (Dorian Depriester)

Voronoï cell are only driven by the distance from its center to those of its neighbours. As a result, cell sizes can not easily be constrained. For instance, Groeber et al. [7] have developped the Constrained Voronoi Tessellation Method (CVTM), consisting in recursively adding new seeds in order to result in realistic cell morphologies.

The Radical Voronoï (RV) tessellation, also known as Laguerre-Voronoï [10], helps to impose the size of each cell through the introduction of a local radius, denoted r. Consider a set of n seeds $\{\boldsymbol{p}_1, \boldsymbol{p}_2, ..., \boldsymbol{p}_n\}$ and a set of n radii $\{r_1, r_2, ..., r_n\}$. For the RV tessellation, (1) becomes:

$$\mathrm{C}_i = \left\{ \boldsymbol{x} \in \Omega \middle| d_{\mathrm{L}}\left(\boldsymbol{x}, \boldsymbol{p}_i, r_i\right) = \min_{k=1}^{n} \left\{ d_{\mathrm{L}}\left(\boldsymbol{x}, \boldsymbol{p}_k, r_k\right) \right\} \right\} \tag{2}$$

where d_{L} denotes the euclidean distance in Laguerre geometry, so that:

$$d_{\mathrm{L}}\left(\boldsymbol{x}, \boldsymbol{p}_k, r_k\right) = \left\| \boldsymbol{x} - \boldsymbol{p}_k \right\|^2 - r_k^2 \,. \tag{3}$$

Consider two cells i and j; according to (2), if

$$\left\| \boldsymbol{p}_i - \boldsymbol{p}_j \right\| = r_i + r_j \tag{4}$$

then the boundary between the two cells is located at the distance r_i (resp. r_j) from $\boldsymbol{p}_i$ (resp. $\boldsymbol{p}_j$). Equation (4) is satisfied if $\boldsymbol{p}_i$ and $\boldsymbol{p}_j$ are the centres of two spheres, in contact with each other, with respective radii r_i and r_j. As a result, the dimensions of the cells resulting from the RV tessellation computed from Random Close Packing (RCP) of spheres are strongly inherited from their radii.

It is worth mentioning that the numerical generation of RCP of spheres is not straightforward. The two main methods used in the literature are the collective rearrangement method [11–15] and the sequential generation. The latter usually consists in numerically pouring a closed volume with the spheres, by simulating a gravitational effect [16–18]. Yang et al. [11] have investigated the evolution of the packing factor of RCPs computed from sphere radii following a lognormal distribution. They have shown that the packing factor was an increasing function of the so-called shape parameter of the distribution (denoted σ below, see subsection 2.1) starting from 0.637. Falco et al. [19] have adapted the "3D-clew" technique [20] to generate the RCPs of sphere. This method consists in adding the spheres one by one into the pack, ensuring the tangency with other spheres. Rodrigues et al. [9] use a virtual container with moving walls instead of gravity. Fan et al. [14] have generated RCPs of spheres by collective rearrangement, in order to investigate the geometry of the RV tessellation thanks to the Qhull software package [21]. They have shown that if the volumes of the spheres follow a lognormal distribution, then those of the resulting RV cells follow a lognormal distribution too. In addition, they have focused on the geometrical characterization of each RV cell. In particular, they have shown that the mean number of faces per RV cell was a decreasing function of the Coefficient of Variation (CV) of sphere volumes, ranging from 13.04 to 14.11. Finally, Fan et al. [14] have investigated the relationship between the CV of the sphere volumes with that of the RV cell volumes.

It is well known that sequential algorithms usually result in anisotropic RCPs [16, 22, 23]. For instance, Tory et al. [16] have reported that the length of projection along the vertical direction (*i.e.* direction of applied

gravitational force) of monodisperse spheres was 11 % greater than those computed along the horizontal directions.

The geometry of a real polycrystalline structure is usually described by the morphology and size of its grains. In order to numerically reproduce those structures using a RV tessellation, it is necessary to predict the adequate distribution for the RCP spheres. Grain sizes can be measured by 3D imaging techniques (such as X-ray tomography or neutron diffraction) but they are more frequently evaluated from 2D cross sections, for instance by microscopy or Electron Backscatter Diffraction (EBSD) mapping. Those 2D observations induce a bias in grain sizes, for they only provide information about the intersection of the 3D grains and the cutting plane. For instance, it can be shown that the mean apparent radius of a sphere with unit radius cut at random latitudes is $\pi/4$ [24]. For polydisperse particles, deriving their 3D sizes from 2D observations is called stereology problem. It is usually solved using an iterative routine applied on finite histograms [25–27]. Lopez-Sanchez and Llana-Fúnez [27] have proposed a routine, namely the two-step method, for the resolution of stereology problems. It consists in:

- deriving the 3D histogram from 2D sections, thanks to the so-called Saltykov method [25];
- fitting a lognormal distribution on the 3D histograms.

The Saltykov method (also known as Scheil-Schwartz-Saltykov method) is an iterative procedure, consisting in evaluating the probability of cutting each grain (considered as spherical) at a certain latitude, resulting in an reduced apparent size. This method is based on the finite histogram (finite number of classes) of apparent sizes. The fundamental assumption is that the upper class (i.e. larger apparent sizes) is given by the largest grains cut near their equatorial planes. When cutting a particle of radius R at a random latitude, the probability of finding an apparent radius r comprised in between r_1 and r_2 is given by:

$$P\left(r_1 < r < r_2\right) = \frac{1}{R}\left(\sqrt{R^2 - r_1^2} - \sqrt{R^2 - r_2^2}\right) . \tag{5}$$

Equation (5) is first used for evaluating the number of grains with radius $R = (r_1 + r_2)/2$, r_1 and r_2 being the limits of the upper class. Then, (5) can be used for each other class to subtract the contribution of grains with size R in the overall histogram. Finally, the previous steps are reiterated, starting from the (remaining) second upper class, and so on.

The aim of this work is to establish continuous inverse functions for predicting the radius distribution parameters (denoted E and σ below) based on 3D or 2D observations. Figure 1 schematically illustrates the method used in this paper for this purpose: RCPs have been computed with different distributions for the sphere radii, then RV tessellations have been carried out on each RCP. Finally, the geometries of the RV cells have been statistically evaluated. The procedure used in this work for generating the geometries is detailed in section 2. Section 3 investigates the geometry of each RCP. A continuous relationship between the radius distribution of the spheres and that of the cell volumes is proposed in this section. In section 4, the bias introduced when one attempt to characterize the grain size from 2D sections is studied and methods

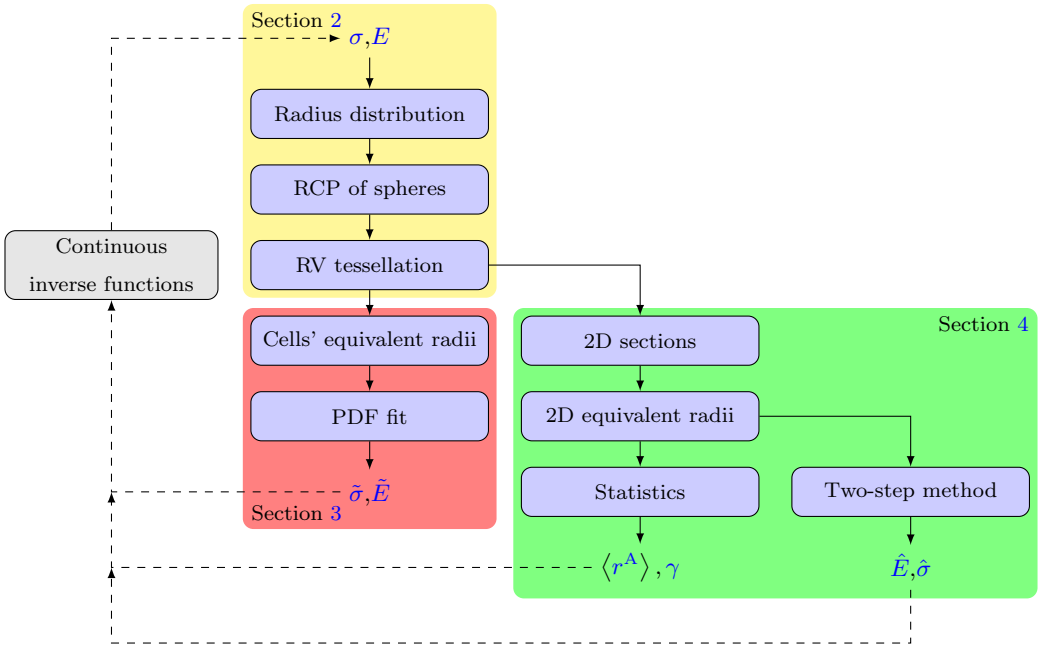

Figure 1: Schematic representation of the method proposed in this paper: the cell size distribution (characterized by $\tilde{\sigma}$ and $\tilde{E}$) results from a distribution of radii (characterized by σ and E) through a sequence of operations. Section 3 investigates the relationship between the sizes of the RV cells and those of the spheres, whereas the apparent sizes in 2D sections are studied in section 4.

for evaluating the 3D distribution based on 2D sections are proposed. In order to assess those methods, a numerical microstructure, representative of a real one, has been generated; those microstructures are compared in section 5.

2. Geometry generation

This section describes the procedure used in this work for generating RCPs of spheres with radii following lognormal distribution, then computing the RV tessellations.

2.1. Radius distribution

Rhines and Patterson [28] have reported that in many polycrystalline materials, the grain volume (denoted V below) distribution follows a lognormal Probability Density Function (PDF), so that:

$$f\left(V \,|\, \mu, \sigma\right) = \frac{1}{V\sigma\sqrt{2\pi}} \exp\left(-\frac{\left(\ln V - \mu\right)^2}{2\sigma^2}\right) \tag{6}$$

with μ and σ the so-called location and shape parameters of the PDF, respectively. The expectation (denoted E below) can be evaluated as follows:

$$E = \exp\left(\mu + \frac{\sigma^2}{2}\right) \tag{7}$$

whereas the coefficient of variation (CV) is:

$$\mathrm{CV} = \sqrt{\exp\left(\sigma^2\right) - 1}\,. \tag{8}$$

It can be shown (see Appendix A) that the sphere volumes follow a lognormal distribution if, and only if, their radii follow a lognormal distribution too. Hence, in this work, all lognormal distributions deal with the radius distribution:

$$f\left(r \,|\, \mu, \sigma\right) = \frac{1}{r\sigma\sqrt{2\pi}} \exp\left(-\frac{\left(\ln r - \mu\right)^2}{2\sigma^2}\right) . \tag{9}$$

Figure 2 illustrates the PDF defined in (9) with $E = 1$.

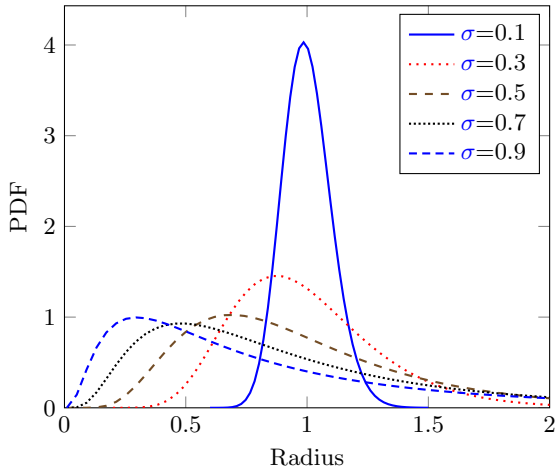

Figure 2: PDF as functions of the radius, for different values of σ: all curves are plotted for $E = 1$.

In this study, geometries have been computed for σ ranging from 0 (monodisperse) to 0.9, such that $E = 1$ (i.e. mean sphere radius equal to 1), that is:

$$\mu = \ln E - \frac{\sigma^2}{2} = -\frac{\sigma^2}{2} . \tag{10}$$

The lognormal distribution (6) has been truncated, keeping 99 % of the whole population (removing tails with a probability cut-off $P_{\text{co}} = 0.5\,\%$) an discretized into 100 bins (see Appendix B for details).

2.2. Generation of the centres

Each RCP of spheres has been generated from the Molecular Dynamic code LAMMPS [29], as illustrated in Figure 3. For those sets, a cubic volume of size $40 \times 40 \times 40$ has been poured by spheres (called atoms in LAMMPS) according to the standard "drop and roll" procedure:

- generate a set of spheres with random radius (with respect to the lognormal PDF) at random locations on top of the volume;
- compute the falls (due to gravitational force) and interactions with other spheres (hard frictionless contact);
- reiterate until the volume is full (when there is no room for new spheres).

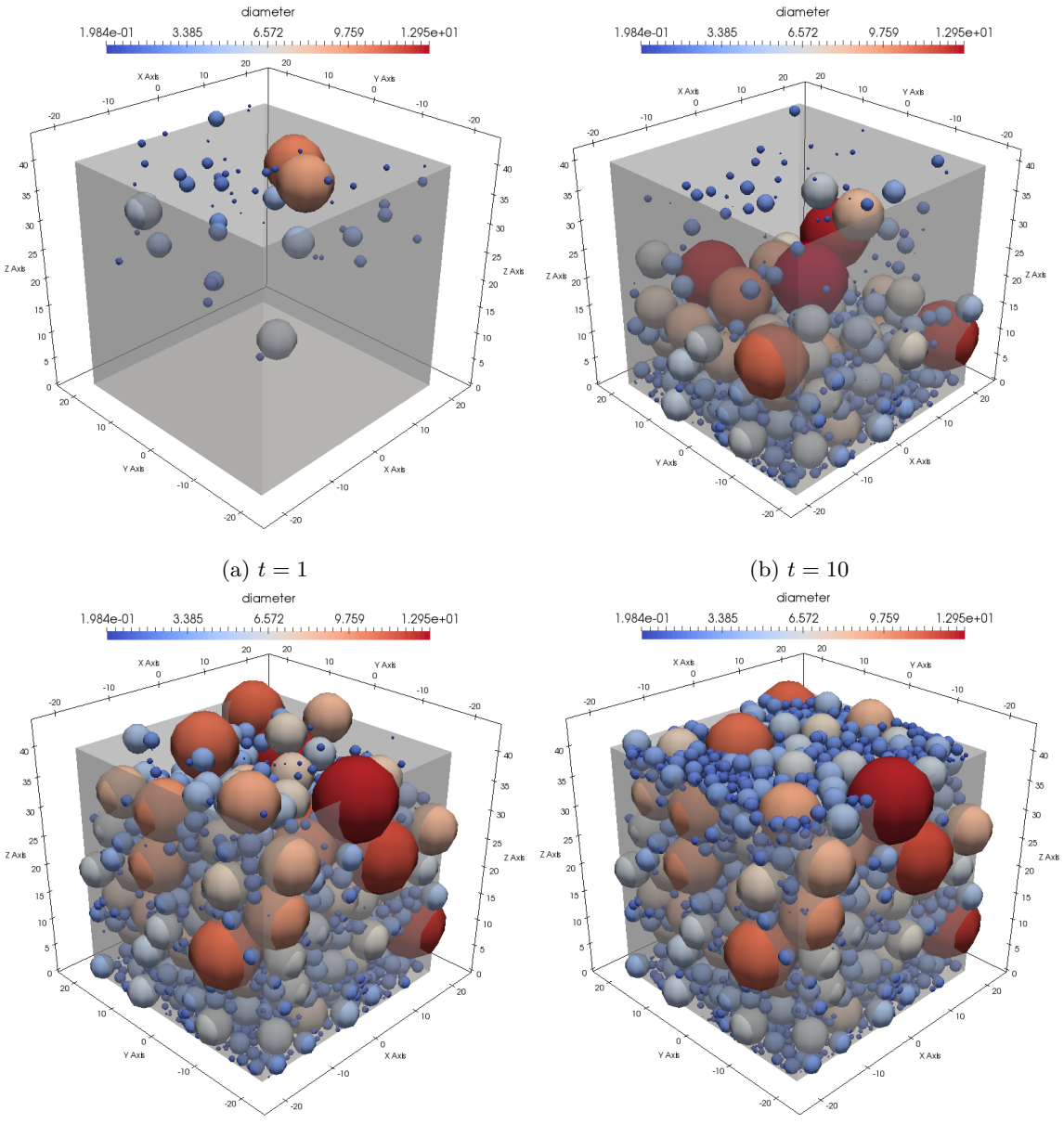

(a) $t = 1$

(b) $t = 10$

(c) $t = 20$

(d) $t = 30$

Figure 3: 3D representation of pouring a closed box (with periodic boundaries on x and y) with $\sigma = 0.9$: each sphere is coloured depending on its diameter.

Let x, y and z be the directions associated to the cubic volume (z being the direction of the gravitational force). For the pouring simulations, the bottom of the volumes ($z = 0$) was considered as a solid wall, so that each sphere was bounded by this plane. On the opposite, periodic boundaries were assumed along the perpendicular directions (x and y). As a result, some spheres appear to interpenetrate the boundaries in Figure 3. The number of spheres in the box ranged from 2737 to 9838 (for $\sigma = 0.9$ and 0, respectively).

Since spheres do not have any physical meaning, their physical properties (such as mass) were arbitrary chosen. Thus, the time step for any pouring simulation (denoted t in Figure 3) can be considered as dimensionless.

2.3. Radical Voronoï tessellation

RV tessellation, based on the center/radius of each packed sphere, has been performed using the `voro++` library [30], as illustrated in Figure 4. In the case of monodisperse spheres ($\sigma = 0$), it is worth mentioning

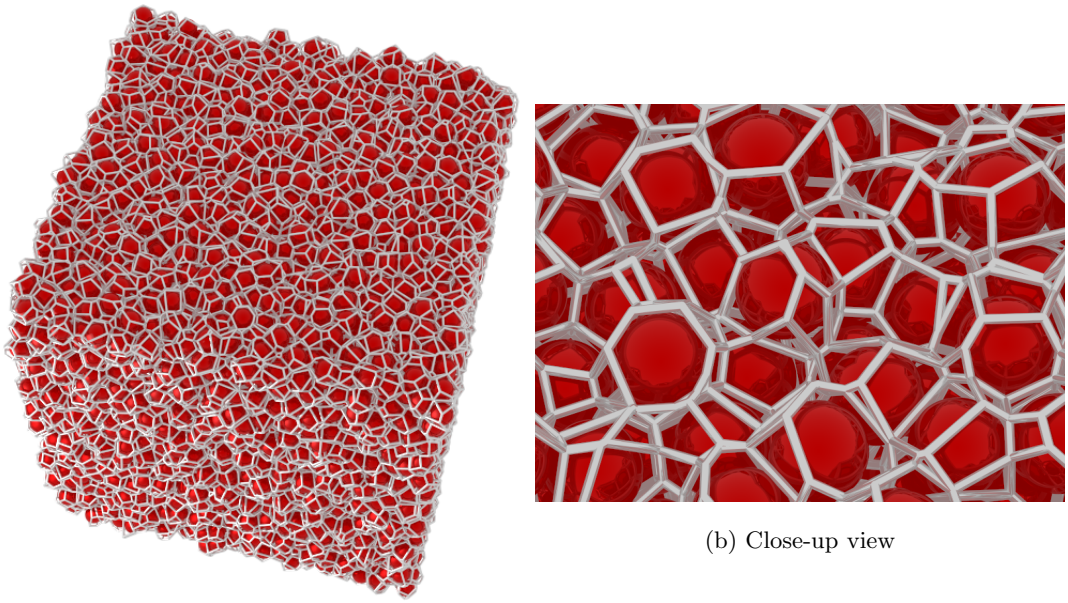

(a) Overall geometry

(b) Close-up view

Figure 4: 3D representation of the RV edges (white) computed from the center of each packed sphere (red) using monodisperse distribution ($\sigma = 0$).

that the RV tessellation acts like a PV one. All domain boundaries (identical to those of the poured box) have been considered as periodic for the tessellation, as evidenced by the non-planar outer surfaces in Figure 4.

3. Analysis of the resulting 3D geometries

In this section, the analysis of the geometries resulting from RV tessellation of each RCP of spheres has led to the following statements:

- the RCPs of spheres generated in this work lead to the same packing factor of that obtained by Fan et al. [14];
- the mean number of faces per RV cell is in good agreement with real grains, found in various granular material;
- the geometry resulting from RV tessellation can be considered as isotropic;
- the equivalent radii of RV cells follows a lognormal distribution if the sphere radii follow a lognormal distribution;
- the relationship between the two aforementioned distributions has been established.

3.1. Packing factor

Each RCP can be characterized in terms of packing factor, that is:

$$\eta = \frac{V_{\text{spheres}}}{V_{\text{box}}}\,. \tag{11}$$

As shown in Figure 5, η is an increasing function of σ, appearing almost linear, ranging from 0.634 to 0.746. In addition, results from Yang et al. [11] are given in Figure 5. Thus, the results are in good agreement, despite the different procedures used for the generation of each RCP.

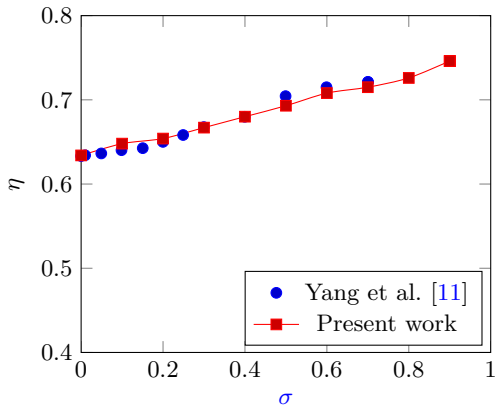

Figure 5: Evolution of the packing factor (η) as function of σ.

3.2. Geometrical properties of RV cells

Figure 6 shows the mean number of faces per RV cell (denoted $\langle N^{\text{f}} \rangle$ below). It appears that $\langle N^{\text{f}} \rangle$ is a decreasing function of σ, starting from 13.7 and equal to 11.3 at $\sigma = 0.9$. Figure 6 also gives the results from Fan et al. [14]. It is clear that the method used in this present work for generating RCP of spheres leads to slightly lower values of $\langle N^{\text{f}} \rangle$ than that used by the latter authors. Nevertheless, the values of $\langle N^{\text{f}} \rangle$ found in this work are in good agreements with real materials, such as β-brass (11.8 [31]), electrolytic iron (12.1 [32]), nickel-base superalloy IN100 (12.9 [33]) and uranium dioxide (14.4 [34]).

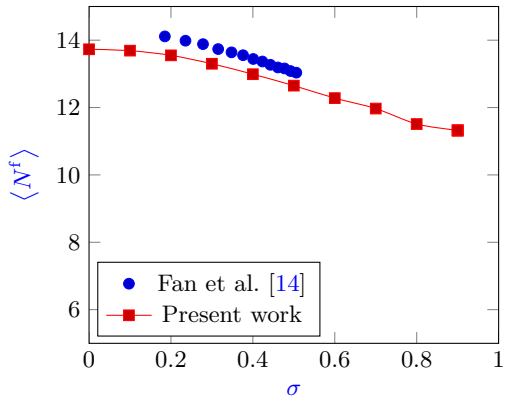

Figure 6: Evolution of the mean number of faces per RV cell ($\langle N^{\mathrm{f}} \rangle$) as function of σ.

The RCPs of spheres generated in this work may be anisotropic [16, 22, 23]. Therefore, attention should be paid about the anisotropy of the RV tessellations. Let Ω be a closed volume, bounded by a surface $\partial\Omega$. Its 5-th Minkowski tensor is defined as follows [35]:

$$\boldsymbol{W} = \frac{1}{3} \int_{\partial\Omega} \boldsymbol{n} \otimes \boldsymbol{n} \mathrm{d}S \tag{12}$$

where $\boldsymbol{n}$ denotes the surface normal and $\otimes$ is the tensor product (that is $(\boldsymbol{n} \otimes \boldsymbol{n})_{k\ell} = n_k n_\ell$). Let $\boldsymbol{W}_i$ be the Minkowski tensor of a given Voronoï cell i, bounded by N_i^{f} faces. It comes:

$$\boldsymbol{W}_i = \frac{1}{3} \sum_{j=1}^{N_i^{\mathrm{f}}} \boldsymbol{n}_j \otimes \boldsymbol{n}_j S_j \tag{13}$$

with S_j and $\boldsymbol{n}_j$ the area and the normal of the j-th face, respectively. The mean Minkowski tensor of a set of p cells, denoted $\langle \boldsymbol{W} \rangle$ below, can be evaluated as follows:

$$\langle \boldsymbol{W} \rangle = \frac{1}{p} \sum_{i=1}^{p} \boldsymbol{W}_i \,. \tag{14}$$

The degree of anisotropy can be expressed as the ratio of the minimal to maximal eigenvalues (denoted $\lambda_{\min}$ and $\lambda_{\max}$, respectively) of the mean Minkowski tensor:

$$\beta = \frac{\lambda_{\min}}{\lambda_{\max}} \,. \tag{15}$$

The degree of anisotropy has been computed in each case, as illustrated in Figure 7. It appears that all the computed geometries can be considered as isotropic, for the related values of β are all close to 1. Nevertheless, this figure shows a drop in isotropy when $\sigma > 0.5$. Larger values of σ have been investigated, leading to even smaller values of β (< 0.95). As a conclusion, the method used here for the generation of RCPs of spheres is only efficient for σ ranging in 0-0.9. In order to investigate larger values of σ, applying a scale factor (of $1/\beta$) on the coordinates along the stacking direction of the cell nodes would help make the resulting geometry isotropic.

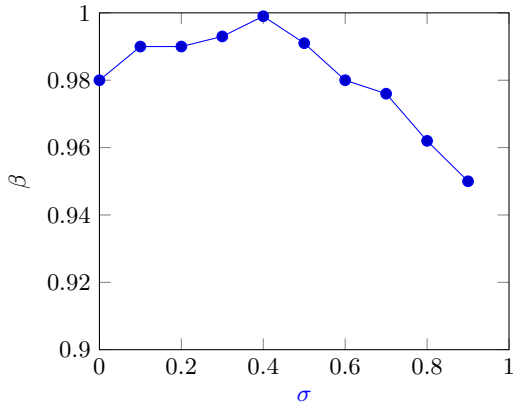

Figure 7: Degree of anisotropy β, as function of σ.

For $\sigma = 0.9$, the mean Minkowski tensor was:

$$\langle \boldsymbol{W} \rangle = \begin{bmatrix} 3.663 & 0.008 & -0.015 \\ 0.008 & 3.656 & 0.007 \\ -0.015 & 0.007 & 3.485 \end{bmatrix} . \tag{16}$$

This tensor can be considered as transverse isotropic, with smaller values along the z direction. This phenomenon can be related to the stacking direction of the spheres.

3.3. Equivalent radii distribution

Considering each Voronoï cell (numbered i) as a sphere, one can define its equivalent radius, denoted r_i^{V}, as function of its volume V_i:

$$r_i^{\mathrm{V}} = \sqrt[3]{\frac{3V_i}{4\pi}} . \tag{17}$$

Figure 8 illustrates the resulting distributions of r^{V} for each investigated value of σ. Both lognormal and gamma PDFs have been fitted on each population. In order to evaluate the goodness-of-fit, the Kolmogorov-Smirnov (KS) test [36] has been performed in each case. Results from the KS tests are plotted in Figure 9 as functions of σ. It appears that for monodisperse spheres ($\sigma = 0$), the proposed PDFs are not well accurate. This discrepancy with Fan et al. [14] may be related to the RCP method used here (*viz.* collective rearrangement *vs.* iterative procedure). On the opposite, the fits are good when $\sigma \neq 0$, specially using the lognormal PDF. According to Figure 9, the lognormal PDF appears to be a good candidate for evaluating the distributions of r^{V}. This result is in agreement with Fan et al. [14]. Thus, only the lognormal PDF will be used hereafter. Figure 8 shows the fitted lognormal PDF in each case (red solid curves).

Let $\tilde{E}$ and $\tilde{\sigma}$ be the expectation and the shape parameters when fitting the lognormal PDF (9) over a given distribution of r^{V}. Figure 10 illustrates the evolutions of $\tilde{E}$ and $\tilde{\sigma}$ as functions of σ. The following statements can be made:

- both $\tilde{\sigma}$ and $\tilde{E}$ are increasing functions of σ;

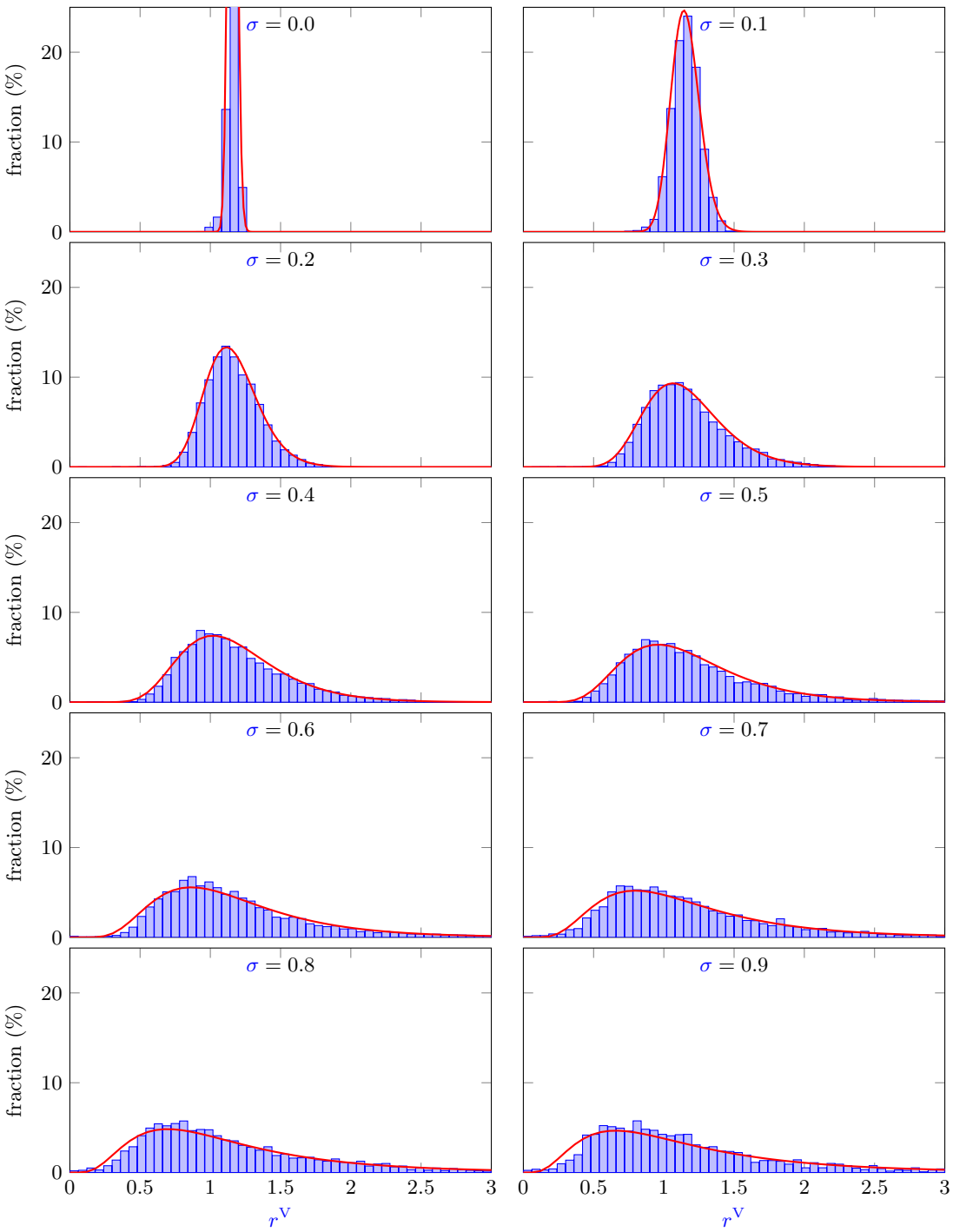

Figure 8: Distributions of the equivalent radius (r^{V}), computed from the cell volumes (3D): the red solid curves illustrate the results from fitting lognormal distributions.

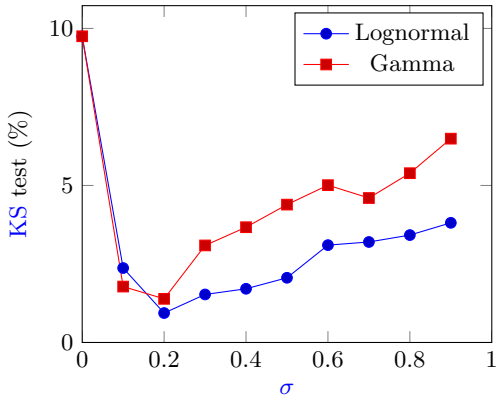

Figure 9: Results from the KS test for the lognormal and gamma distribution, as functions of σ.

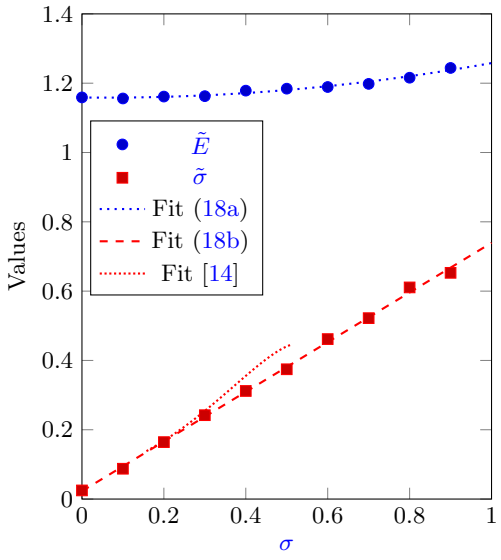

Figure 10: Evolutions of the lognormal PDF parameters computed from cell volumes ($\tilde{E}$ and $\tilde{\sigma}$): as a comparison, the fit given by Fan et al. [14] has been plotted too.

- the mean equivalent radius is always larger than the mean sphere radius ($\tilde{E} > E$);
- the resulting shape parameter $\tilde{\sigma}$ is always smaller than that of the sphere radii ($\tilde{\sigma} < \sigma$).

The following polynomial regressions can be established:

$$\tilde{E} = 0.1123\sigma^2 - 0.013\sigma + 1.1587\,; \tag{18a}$$

$$\tilde{\sigma} = 0.7166\sigma + 0.0228 \tag{18b}$$

with respective coefficients of determination $R^2 = 0.9748$ and 0.999. Figure 10 also helps to compare the fit given in (18b) with that given by Fan et al. [14]. In its definition domain ($0.15 < \sigma < 0.51$), the latter is in good agreement with the present fit. Since the investigated distributions for the sphere radii were chosen such that $E = 1$, a scale factor can be applied on (18a) to make it suitable for any given value of E, that is:

$$\frac{\tilde{E}}{E} = 0.1123\sigma^2 - 0.013\sigma + 1.1587\,. \tag{19}$$

As a result, based on a given distribution of equivalent radii, one can evaluate the PDF parameters to be used for the sphere radii, according to the following procedure:

1. fit the distribution with a lognormal PDF (leading to $\tilde{E}$ and $\tilde{\sigma}$);
2. evaluate σ by solving (18b);
3. compute E using (19).

The whole procedure for numerically generating a 3D geometry is summed up in Figure 11.

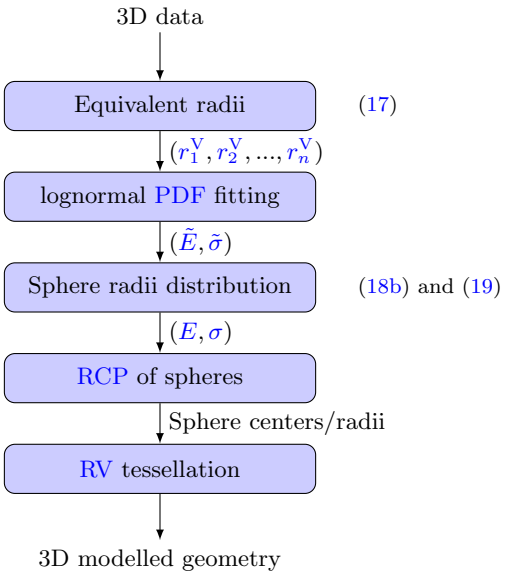

Figure 11: Schematic representation of the method proposed in section 3 for numerically generating a 3D polycrystal representative of a real one. As a remainder, references to the *ad hoc* equations are also given.

4. Stereology problem

In this section, 2D slicing has been performed on each RCP in order to study the bias introduced when one tries to evaluate the grain size based on 2D sections. The following statement are made:

- the apparent radii distributions can be characterized using both the mean value ($\langle r^{\mathrm{A}} \rangle$) and the Pearson's second skewness coefficient (γ);
- relationships between both $\langle r^{\mathrm{A}} \rangle$ and γ *versus* σ can be established;
- the accuracy of the two-step method [27] has been investigated. It has been shown that this method overestimates both the expectation and the shape parameter for the cell sizes;
- a method is proposed to derive the values of σ and E thanks to the two-step method;
- the morphology of the 2D sections appears to be statistically independent of the slicing direction.

4.1. 2D sections of the RV tessellations

In order to evaluate the bias introduced by the stereology problem, 20 parallel cuts of each volume have been computed along each frame direction (x, y and z), as performed by Falco et al. [19]. Examples of 2D sections are given in Figure 12. One can evaluate the equivalent radius (r_i^{A}) of an apparent 2D grain i, based

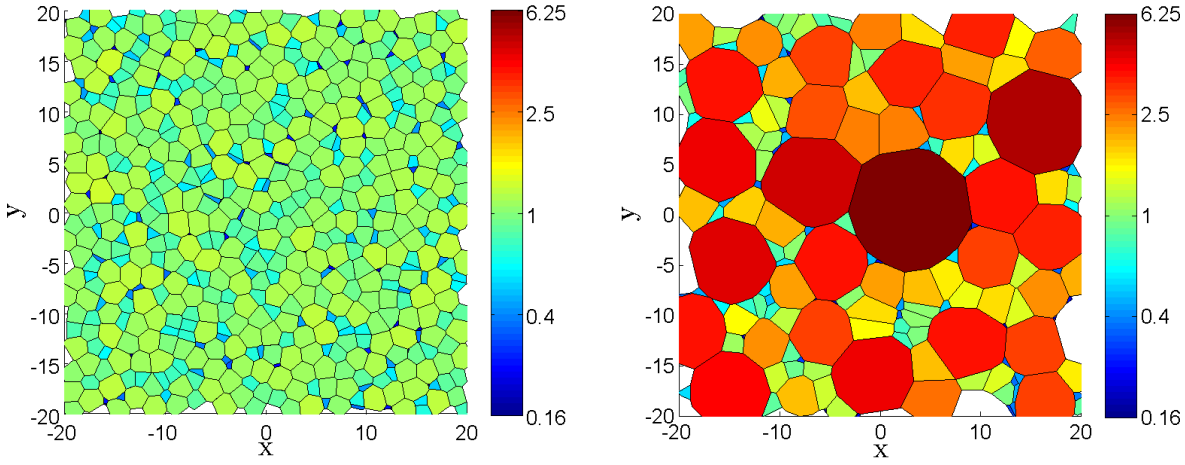

(a) $\sigma = 0$ (b) $\sigma = 0.9$

Figure 12: 2D sections of the Voronoï cells computed from RCP of spheres (cut plane: $z = 20$): each grain is coloured as function of its the equivalent radius (r^{A}) in log scale.

on its surface area (A_i) [27]:

$$r_i^{\mathrm{A}} = \sqrt{\frac{A_i}{\pi}}\,. \tag{20}$$

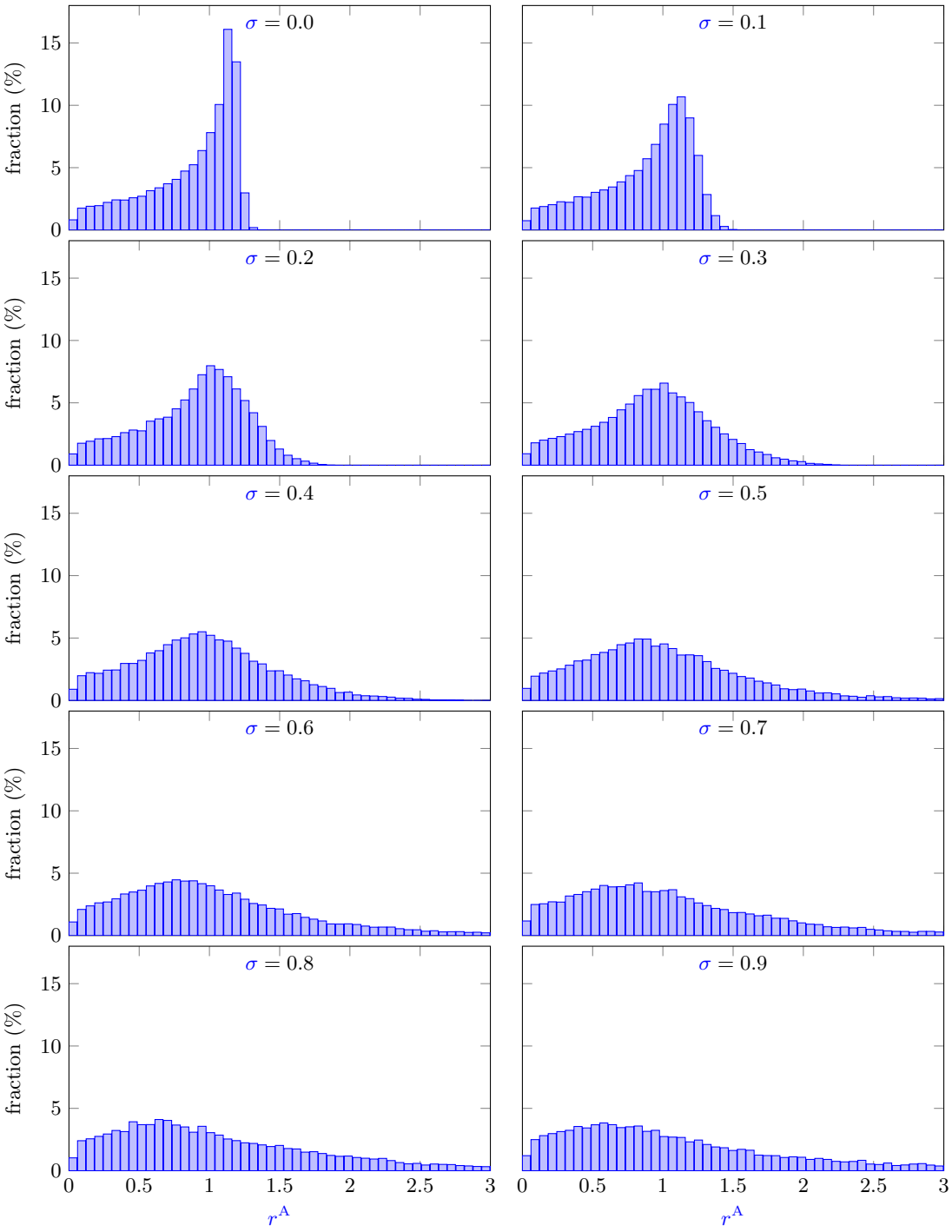

Figure 13: Distributions of the equivalent radius, computed from 2D slices (r^{A}).

4.2. 2D Distribution of apparent sizes

Figure 13 shows the distributions of r^{A} for each set of geometries with given value of σ. Compared to the distribution of r^{V} (given in Figure 8), this figure displays a large variety of distributions, characterized by a large peak at lower values of σ and a remarkable skewness effect.

The shape of the distributions can be characterized by the Pearson's second skewness coefficient γ [37], as a function of the mean and median values and the standard deviation:

$$\gamma = 3\frac{\text{mean} - \text{median}}{\text{standard deviation}}\,. \tag{21}$$

Figure 14 shows the evolutions of the arithmetic mean value of r^{A} (denoted $\langle r^{\mathrm{A}}\rangle$ below) and the skewness factor. It appears that they are both increasing functions of σ. In addition, the distribution of r^{A} appears

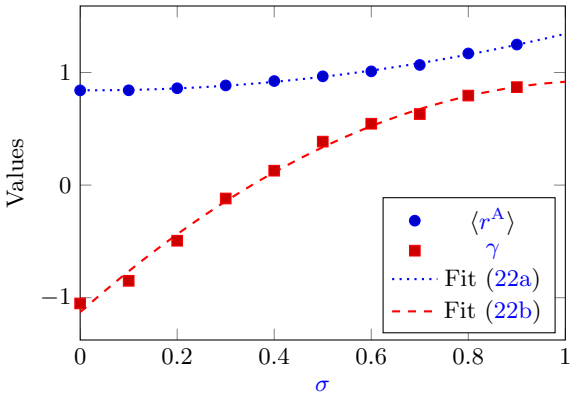

Figure 14: Evolutions of the mean apparent grain size ($\langle r^{\mathrm{A}}\rangle$) and distribution skewness (γ), as functions of σ.

skewed left ($\gamma < 0$) if $\sigma < 0.4$, skewed right otherwise. Second order polynomial curves have been fitted onto the datasets presented in Figure 14 ($\langle r^{\mathrm{A}}\rangle$ and γ *vs.* σ), leading to good correlations ($R^2 = 0.997$ and 0.995, respectively) and the following relationships:

$$\frac{\langle r^{\mathrm{A}}\rangle}{E} = \quad 0.5242\sigma^2 - 0.0231\sigma + 0.8422\,; \tag{22a}$$

$$\gamma = -1.7678\sigma^2 + 3.8140\sigma - 1.1284\,. \tag{22b}$$

As a result, equations (22) help to evaluate the PDF parameters to be used when one attempts to generate a 3D polycrystal based on a 2D section. The method proposed here, called γ-r^{A} hereafter, is summed up in Figure 15.

For monodisperse spheres ($\sigma = 0$), equations (22a) and (19) give a ratio of $\langle r^{\mathrm{A}}\rangle$ to $\tilde{E}$ equal to 0.73. This value is slightly smaller than the theoretical one for monodisperse spherical particles ($\pi/4 \approx 0.79$ [24]). This discrepancy may be because the cells are not spherical and not fully monodisperse ($\tilde{\sigma} = 0.0249$).

4.3. Resolution of the stereology problem using the two-step method

Based on the sets of 2D sections (as detailed in subsection 4.1), the distributions of volumetric equivalent radii (r^{V}) have been derived from the distributions of area-based equivalent radii (r^{A}) presented in Figure 13.

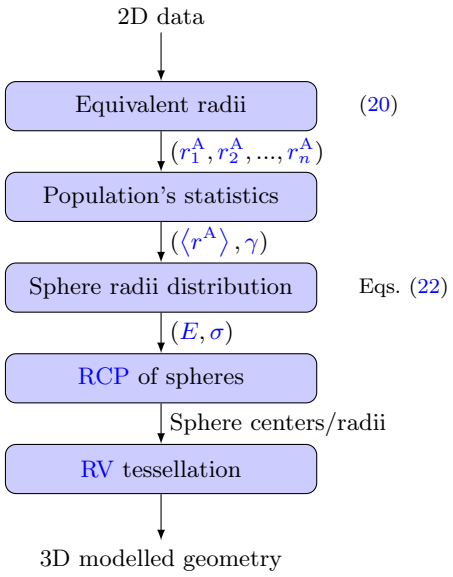

Figure 15: Schematic representation of the method proposed in subsection 4.2 (namely the γ-r^{A} method) for numerically generating a 3D polycrystal representative of a real one, based on a 2D cross-section. As a remainder, references to the *ad hoc* equations are also given.

In this work, the aforementioned two-step method [27] has been used to evaluate the PDF parameters in (9). Let $\hat{E}$ and $\hat{\sigma}$ be the expectation and the shape parameters found using this method. Figure 16 shows the values of $\hat{E}$ and $\hat{\sigma}$ as functions of σ. In addition, the corresponding values of $\tilde{E}$ and $\tilde{\sigma}$ have been presented in this figure (introduced in Figure 2) for the sake of comparison. It appears that the results from the two-step method are in good agreements with the actual data only for smaller values of σ. Indeed, the two-step method overestimates both expectation and shape parameter (with mean relative errors of 9 and 45 %, respectively). A second order polynomial function has been fitted on $\hat{E}$ (with $R^2 = 0.953$) whereas a linear function has been fitted on $\tilde{\sigma}$ (with $R^2 = 0.990$). As a result, the following relationships can be established:

$$\frac{\hat{E}}{E} = 0.2225\sigma^2 + 0.1749\sigma + 1.1505\,; \tag{23a}$$

$$\hat{\sigma} = 1.0184\sigma \ + 0.0341\,. \tag{23b}$$

As a conclusion, applying the two-step method then solving equations (23) lead to both σ and E. Thus, this procedure, called the three-step method hereafter, is summed up in Figure 17.

4.4. Influence of slicing direction

In order to evaluate if the cutting direction have any influence on the 2D grain statistics, three scalar values have been computed from each set of parallel cuts:

- arithmetic mean value of the apparent radius ($\langle r^{\mathrm{A}} \rangle$);

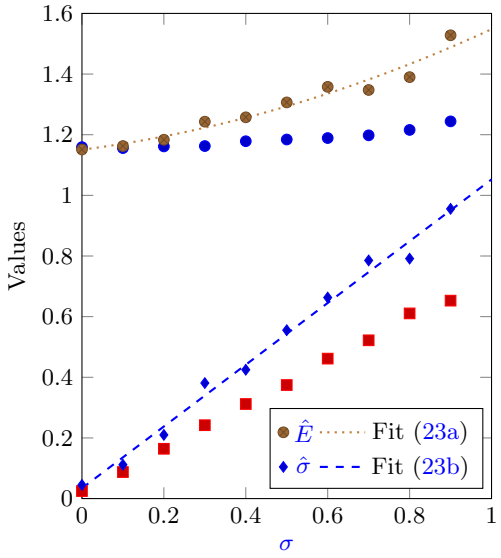

Figure 16: Evolutions of the unfolded expectation ($\hat{E}$) and shape parameter ($\hat{\sigma}$) found using the two-step method [27] as functions of σ. As a comparison, values of $\tilde{E}$ (●) and $\tilde{\sigma}$ (■) are plotted too.

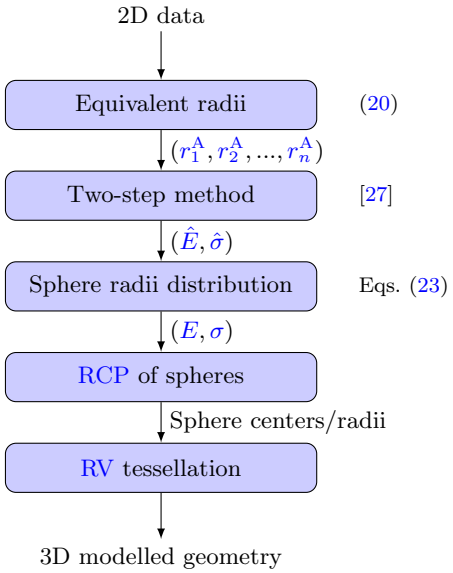

Figure 17: Schematic representation of the method proposed in subsection 4.3 (namely the three-step method) for numerically generating a 3D polycrystal representative of a real one, based on a 2D cross-section. As a remainder, references to the *ad hoc* equations/paper are also given.

- area-weighted mean radius:

$$\left\langle r^{\mathrm{A}} \right\rangle_{\mathrm{area}} = \frac{1}{\sum_i A_i} \sum_i r_i^{\mathrm{A}} A_i = \frac{\sum_i A_i^{3/2}}{\sqrt{\pi} \sum_i A_i} \tag{24}$$

- mean Aspect Ratio (AR) of the apparent grains.

The latter has been computed by first fitting an ellipse onto the vertices of each apparent grain. Then, it has been considered that the AR of the apparent grain was equal to that of the ellipse (i.e. major to minor axes ratio). Figure 18 shows the evolution of those three scalar descriptors, computed for each set of parallel cuts and each geometry. In each case, the mean AR is relatively small, evidencing that each cut appears

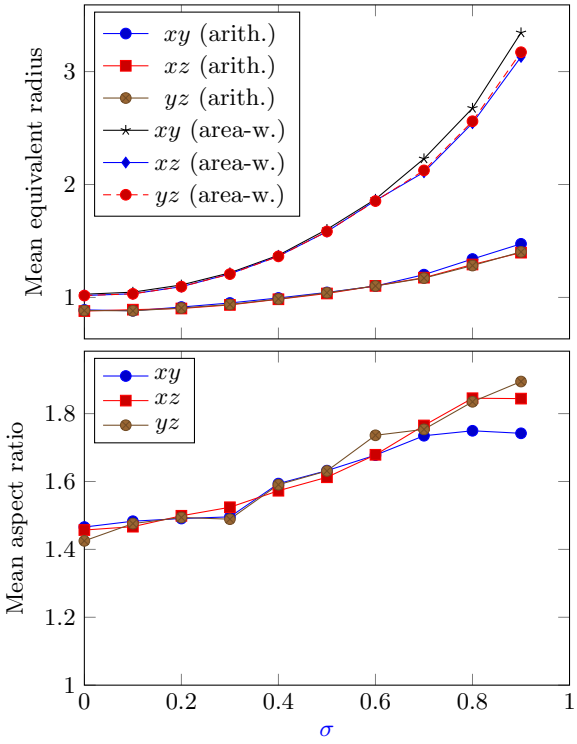

Figure 18: Arithmetic mean equivalent radius, area-weighted mean equivalent radius and aspect ratios computed from each set of parallel slices, as functions of σ.

equiaxed. For a given descriptor, all curves appear almost superimposed, specially when $\sigma \leq 0.6$, suggesting that the apparent grains are independent of the cutting direction. This result is in accordance with the isotropy reported in subsection 3.2.

Figure 18 also shows that the larger σ is, the larger the area-weighted mean radius is, compared to the arithmetic mean. This results is emphasized in Figure 12b, where large grains seem to be dominants whereas the arithmetic mean is only 1.248.

5. Application on a real polycrystalline microstructure

In this section, the methods proposed in section 4 to numerically generate a 3D polycrystal, based on a 2D section of a real material, are tested. The following statements are made:

- both the γ-r^{A} and the three-step methods give valuable results;
- the three-step methods appears to be more accurate in terms of equivalent radii distribution.

5.1. Material

Uranium Dioxide (UO_2) has been used as an application material. It was manufactured by sintering, resulting in an homogeneous and equiaxed structure. The orientation map[1], obtained using the EBSD technique was of size 1200 µm × 320 µm (with step size 2 µm). The MTEX toolbox [38] has been used to reconstruct each grain using a misorientation threshold of 5°. Then, all grains neighbouring the domain were removed, as illustrated in Figure 19. As a result, statistics were performed on 4264 grains.

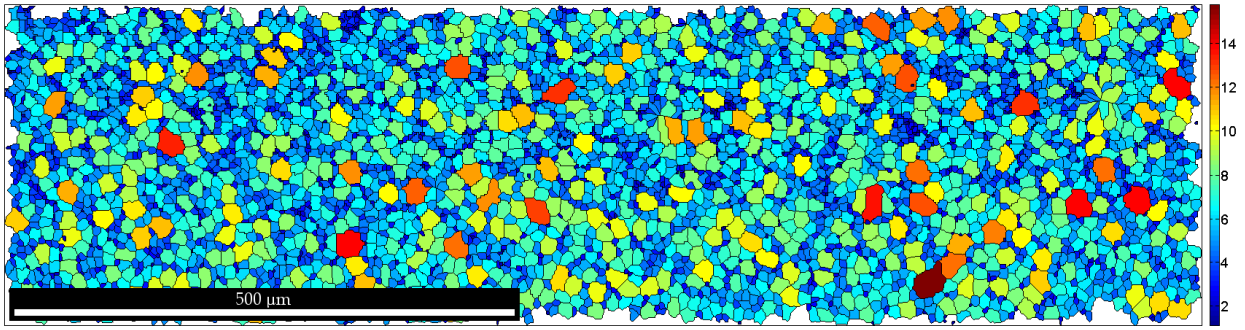

Figure 19: Reconstructed grains in UO_2: the colour indicates the corresponding equivalent radius (µm).

The geometry of each grain has been used to compute its equivalent radius. Then, the grain size distribution has been investigated, as illustrated in Figure 20.

5.2. Analysis of the microstructure's geometric descriptors and 3D tessellation

The mean equivalent radius was 4.694 µm and the skewness factor was $\gamma = 0.350$. Therefore, the γ-r^{A} method (22) results in $E = 4.863$ µm and $\sigma = 0.507$.

The two-step method [27] applied on the distribution given in Figure 20 results in $\hat{E} = 5.651$ µm and $\hat{\sigma} = 0.462$. Therefore, the three-step method (23) results in $E = 4.473$ µm and $\sigma = 0.420$.

RCP of spheres has been computed for each pair (E,σ) identified above. Then, RV tessellations have been performed on each RCP.

[1] Courtesy of Soulacroix [34].

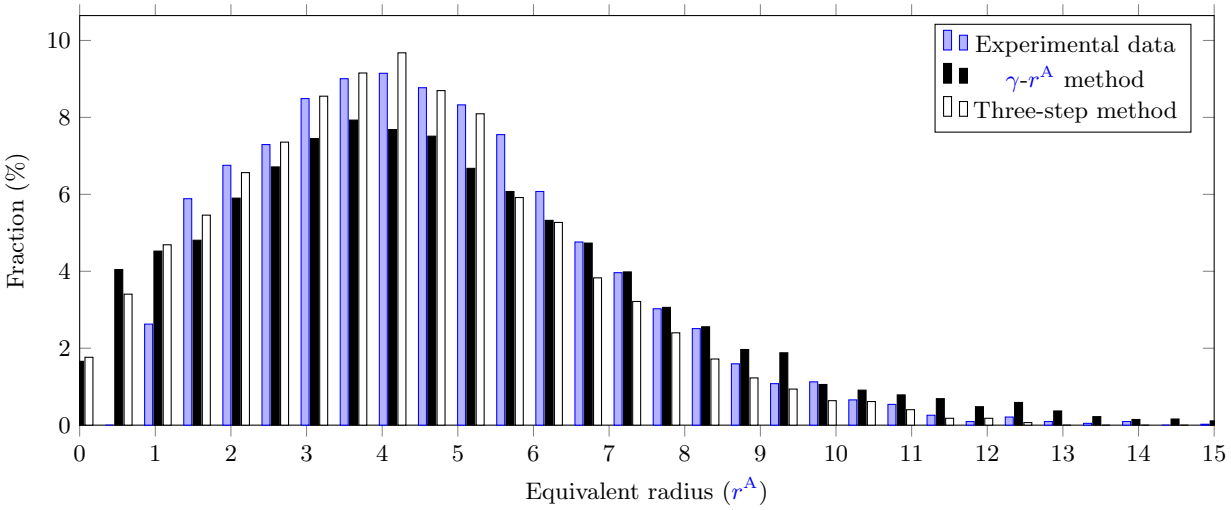

Figure 20: Distribution of the equivalent radius in the UO_2: radii computed from EBSD data as compared to those found in 2D slices of RCP-based RV tessellations.

5.3. Discussion

In order to compare the results from RV tessellations with the experimental data, series of parallel sections have been carried out, as detailed in subsection 4.1. More than 8000 2D grains were found in each tessellation. Examples of 2D sections are given in Figure 21.

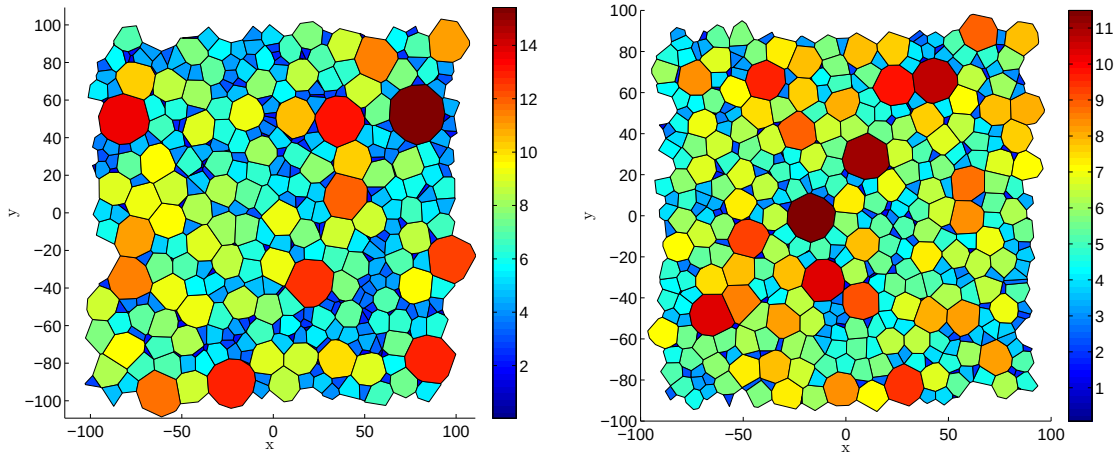

(a) γ-r^A method.

(b) Three-step method.

Figure 21: 2D cuts of the 3D geometry generated based on the EBSD map: the colour indicates the corresponding radius.

From each series, the corresponding distribution of equivalent radii (r^A) has been studied, as illustrated in Figure 20. It appears that the simulated distributions fit well with that from the EBSD map in terms of sharpness and mode (location of the maximum). For EBSD measurements, the minimum grain area was $4\,\mu m^2$ (because of the dot size), leading to a minimum equivalent radius of $1.13\,\mu m$. On the opposite, there was no lower bound for the grain sizes computed from generated data (except round-off errors of double-

precision floating-point). This explains the discrepancy in the distributions given in Figure 21 for lower values of r^{A}. In order to evaluate the goodness between those distributions, some metrics have been used, as summed up in Table 1. It appears that the γ-r^{A} method leads to good prediction of the arithmetic mean but

Table 1: Scalar parameters describing the radius distributions presented in Figure 20 (µm).

		Method	
	Expe.	γ-r^{A}	three-step
Arithme. mean	4.694	4.678	4.196
Area-wt. mean	6.742	7.647	6.357
Standard dev.	2.244	2.781	2.268

it slightly overestimates both the area-weighted mean grain size and standard deviation. On the opposite, the three-step method results in higher accuracy in terms of area-weighted mean radius and standard deviation. Since experimental polycrystalline microstructures are usually described by the area-weighted mean grain size rather than the arithmetic mean grain size, the three-step method may be more accurate than the γ-r^{A} method.

6. Conclusion

RCPs of spheres have been generated in LAMMPS, with radii following a lognormal distribution for a shape parameter (σ) ranging from 0 to 0.9 and unit expectation ($E = 1$). From each pack, the RV tessellation has been performed. Then, efforts have been made to find an analytical continuous correlation between the resulting geometry and the input parameters (shape parameter and expectation).

If one tries to numerically generate a polycrystalline aggregate knowing the grain volume distribution of a given material, the following steps are proposed:

1. evaluate the equivalent radii, as defined in (17);
2. fit a lognormal PDF on the distribution (i.e. identify $\tilde{E}$ and $\tilde{\sigma}$);
3. evaluate the corresponding parameters for the sphere radius distribution, based on (19) and (18b).

If one tries to numerically generate a polycrystal from a 2D cross-section (e.g. thanks to EBSD analysis), two methods are proposed. First, they both consist in:

1. computing the area of each apparent grain;
2. evaluating the equivalent radii, as defined in (20).

Then, one can either:

- evaluate σ (by solving (22b)), then E (using (22a));

- derive a lognormal PDF on the distribution (i.e. identify $\hat{E}$ and $\hat{\sigma}$) using the two-step method [27], then evaluate the corresponding parameters for the sphere radii distribution, based on equations (23).

Finally, one can compute the RCP of spheres and perform the RV tessellation. It has been shown that the geometry resulting from the RV tessellation can be considered as isotropic if $\sigma < 0.9$.

A microstructure taken from a real material (uranium dioxide manufactured by sintering) has been reproduced using the proposed methods. It has been shown that they both lead to good correlation with experimental data in terms of size distribution. The method involving the resolution of the stereology problem (two-step method) has resulted in higher accuracy.

References

[1] F. Barbe, L. Decker, D. Jeulin, G. Cailletaud, Intergranular and intragranular behavior of polycrystalline aggregates. Part 1: F.E. model, International Journal of Plasticity 17 (2001) 513 – 536.

[2] R. Quey, P. Dawson, F. Barbe, Large-scale 3D random polycrystals for the finite element method: Generation, meshing and remeshing, Computer Methods in Applied Mechanics and Engineering 200 (2011) 1729 – 1745.

[3] M. A. Groeber, M. A. Jackson, DREAM.3D: A digital representation environment for the analysis of microstructure in 3D, Integrating Materials and Manufacturing Innovation 3 (2014) 5.

[4] A. Okabe, Spatial tessellations, Wiley Online Library, 1992.

[5] J. Fleig, The grain boundary impedance of random microstructures: numerical simulations and implications for the analysis of experimental data, Solid State Ionics 150 (2002) 181 – 193. Ringberg Workshop 2000 Special Issue.

[6] K. Zhang, M. Wu, R. Feng, Simulation of microplasticity-induced deformation in uniaxially strained ceramics by 3-D Voronoi polycrystal modeling, International Journal of Plasticity 21 (2005) 801 – 834.

[7] M. Groeber, S. Ghosh, M. D. Uchic, D. M. Dimiduk, A framework for automated analysis and simulation of 3D polycrystalline microstructures. part 2: Synthetic structure generation, Acta Materialia 56 (2008) 1274 – 1287.

[8] F. Fritzen, T. Böhlke, E. Schnack, Periodic three-dimensional mesh generation for crystalline aggregates based on voronoi tessellations, Computational Mechanics 43 (2009) 701–713.

[9] A. M. Rodrigues, F. Bardella, M. K. Zuffo, R. M. L. Neto, Integrated approach for geometric modeling and interactive visual analysis of grain structures, Computer-Aided Design 97 (2018) 1 – 14.

[10] F. Aurenhammer, Power diagrams: properties, algorithms and applications, SIAM Journal on Computing 16 (1987) 78–96.

[11] A. Yang, C. Miller, L. Turcoliver, Simulation of correlated and uncorrelated packing of random size spheres, Physical review E 53 (1996) 1516.

[12] L. Liu, Z. Zhang, A. Yu, Dynamic simulation of the centripetal packing of mono-sized spheres, Physica A: Statistical Mechanics and its Applications 268 (1999) 433–453.

[13] Y. Wu, Z. Fan, Y. Lu, Bulk and interior packing densities of random close packing of hard spheres, Journal of Materials Science 38 (2003) 2019–2025.

[14] Z. Fan, Y. Wu, X. Zhao, Y. Lu, Simulation of polycrystalline structure with voronoi diagram in laguerre geometry based on random closed packing of spheres, Computational Materials Science 29 (2004) 301 – 308.

[15] R. S. Farr, R. D. Groot, Close packing density of polydisperse hard spheres, The Journal of chemical physics 131 (2009) 244104.

[16] E. M. Tory, B. H. Church, M. K. Tam, M. Ratner, Simulated random packing of equal spheres, The Canadian Journal of Chemical Engineering 51 (1973) 484–493.

[17] L. E. Silbert, D. Ertaş, G. S. Grest, T. C. Halsey, D. Levine, Geometry of frictionless and frictional sphere packings, Physical Review E 65 (2002) 031304.

[18] M. M. Roozbahani, B. B. Huat, A. Asadi, Effect of rectangular container's sides on porosity for equal-sized sphere packing, Powder Technology 224 (2012) 46 – 50.

[19] S. Falco, J. Jiang, F. D. Cola, N. Petrinic, Generation of 3D polycrystalline microstructures with a conditioned laguerre-voronoi tessellation technique, Computational Materials Science 136 (2017) 20 – 28.

[20] F. De Cola, S. Falco, E. Barbieri, N. Petrinic, New 3D geometrical deposition methods for efficient packing of spheres based on tangency, International Journal for Numerical Methods in Engineering 104 (2015) 1085–1114. Nme.4955.

[21] C. B. Barber, D. P. Dobkin, H. Huhdanpaa, The Quickhull algorithm for convex hulls, ACM Trans. Math. Softw. 22 (1996) 469–483.

[22] E. Tory, N. Cochrane, S. Waddell, Anisotropy in simulated random packing of equal spheres, Nature 220 (1968) 1023.

[23] A. Bezrukov, M. Bargiel, D. Stoyan, et al., Statistical analysis of simulated random packings of spheres, Particle & Particle Systems Characterization 19 (2002) 111.

[24] P. Goldsmith, The calculation of true particle size distributions from the sizes observed in a thin slice, British Journal of Applied Physics 18 (1967) 813.

[25] M. D. Higgins, Measurement of crystal size distributions, American Mineralogist 85 (2000) 1105–1116.

[26] D. L. Sahagian, A. A. Proussevitch, 3D particle size distributions from 2D observations: stereology for natural applications, Journal of Volcanology and Geothermal Research 84 (1998) 173–196.

[27] M. A. Lopez-Sanchez, S. Llana-Fúnez, An extension of the Saltykov method to quantify 3D grain size distributions in mylonites, Journal of Structural Geology 93 (2016) 149 – 161.

[28] F. Rhines, B. Patterson, Effect of the degree of prior cold work on the grain volume distribution and the rate of grain growth of recrystallized aluminum, Metallurgical Transactions A 13 (1982) 985–993.

[29] S. Plimpton, Fast parallel algorithms for short-range molecular dynamics, Journal of computational physics 117 (1995) 1–19.

[30] C. Rycroft, Voro++: A three-dimensional voronoi cell library in C++, Lawrence Berkeley National Laboratory (2009).

[31] C. Xie, S. Ghosh, M. Groeber, Modeling cyclic deformation of hsla steels using crystal plasticity, Journal of engineering materials and technology 126 (2004) 339–352.

[32] C. Zhang, M. Enomoto, A. Suzuki, T. Ishimaru, Characterization of three-dimensional grain structure in polycrystalline iron by serial sectioning, Metallurgical and Materials Transactions A 35 (2004) 1927–1933.

[33] M. Groeber, S. Ghosh, M. D. Uchic, D. M. Dimiduk, A framework for automated analysis and simulation of 3D polycrystalline microstructures.: Part 1: Statistical characterization, Acta Materialia 56 (2008) 1257 – 1273.

[34] J. Soulacroix, Approche micromécanique du comportement du combustible dioxyde d'uranium, Ph.D. thesis, École Nationale Supérieure d'Arts et Métiers, 2014. 2014ENAM0032.

[35] G. E. Schrder-Turk, W. Mickel, S. C. Kapfer, M. A. Klatt, F. M. Schaller, M. J. F. Hoffmann, N. Kleppmann, P. Armstrong, A. Inayat, D. Hug, M. Reichelsdorfer, W. Peukert, W. Schwieger, K. Mecke, Minkowski Tensor Shape Analysis of Cellular, Granular and Porous Structures, Advanced Materials 23 (2011) 2535–2553.

[36] F. J. Massey Jr, The Kolmogorov-Smirnov test for goodness of fit, Journal of the American statistical Association 46 (1951) 68–78.

[37] D. P. Doane, L. E. Seward, Measuring skewness: a forgotten statistic, Journal of Statistics Education 19 (2011) 1–18.

[38] F. Bachmann, R. Hielscher, H. Schaeben, Texture analysis with MTEX–free and open source software toolbox, in: Solid State Phenomena, volume 160, Trans Tech Publ, 2010, pp. 63–68.

Appendix A. Relationship between radius and volume distributions of spheres

For spheres, (6) can be rewritten depending on their radii:

$$f\left(V \,|\, \mu, \sigma\right) = f\left(\frac{4\pi}{3} r^3 \,\middle|\, \mu, \sigma\right) \tag{A.1}$$

Let $g\left(r \,|\, \mu, \sigma\right)$ be the PDF associated to r. A change on variable must conserve differential probability:

$$g\left(r \,|\, \mu, \sigma\right) \mathrm{d}r = f\left(V \,|\, \mu, \sigma\right) \mathrm{d}V \tag{A.2}$$

$$= f\left(\frac{4\pi}{3} r^3 \,\middle|\, \mu, \sigma\right) \mathrm{d}\left(\frac{4\pi}{3} r^3\right) \tag{A.3}$$

$$\Leftrightarrow \qquad g\left(r \,|\, \mu, \sigma\right) = 4\pi r^2 f\left(\frac{4\pi}{3} r^3 \,\middle|\, \mu, \sigma\right) . \tag{A.4}$$

Equations (6) and (A.4) lead to:

$$\begin{aligned} g\left(r \,|\, \mu, \sigma\right) &= \frac{1}{\frac{1}{3} r \sigma \sqrt{2\pi}} \exp\left(-\frac{\left(3 \ln r + \ln\left(4\pi/3\right) - \mu\right)^2}{2\sigma^2}\right) \\ &= \frac{1}{R \sigma' \sqrt{2\pi}} \exp\left(-\frac{\left(\ln r - \mu'\right)^2}{2\left(\sigma'\right)^2}\right) \end{aligned} \tag{A.5}$$

with:

$$\sigma' = \frac{\sigma}{3} ; \tag{A.6a}$$

$$\mu' = \frac{\mu - \ln\left(4\pi/3\right)}{3} . \tag{A.6b}$$

Appendix B. Discretization of the lognormal PDF

Since LAMMPS only works with a limited number of possible sphere radii, the continuous PDF must be converted into a finite histogram. The Cumulative Density Function (CDF) for the lognormal distribution is:

$$F\left(r \,|\, \mu, \sigma\right) = \frac{1}{2}\left[1 + \mathrm{erf}\left(\frac{\ln r - \mu}{\sigma\sqrt{2}}\right)\right] , \tag{B.1}$$

erf being the error function. Let P_{co} be the probability cut-off value and $r_{\min}$ and $r_{\max}$ be the corresponding truncating limits, so that:

$$P\left(r < r_{\min}\right) = P_{\mathrm{co}} ; \tag{B.2a}$$

$$P\left(r > r_{\max}\right) = P_{\mathrm{co}} . \tag{B.2b}$$

Equation (B.1) gives:

$$r_{\min} = \exp\left(-\sigma\sqrt{2}\,\mathrm{erf}^{-1}\left(1 - 2P_{\mathrm{co}}\right) + \mu\right) ; \tag{B.3a}$$

$$r_{\max} = \exp\left(\ \ \sigma\sqrt{2}\,\mathrm{erf}^{-1}\left(1 - 2P_{\mathrm{co}}\right) + \mu\right) , \tag{B.3b}$$

erf^{-1} being the inverse error function. The truncated PDF can be discretized into n equally spaced bins. Let r_i be the mid-location of the i-th bin; it comes:

$$r_i = r_{\min} + \left(i - \frac{1}{2}\right)\Delta r \quad \text{with: } \Delta r = \frac{r_{\max} - r_{\min}}{n}\,. \tag{B.4}$$

According to (B.1) and (B.2), the normalized discrete probability of finding a sphere with radius r_i is:

$$P\left(r_i\right) = \frac{P_i^+ - P_i^-}{2\left(1 - 2P_{\mathrm{co}}\right)} \tag{B.5}$$

with:

$$P_i^+ = \mathrm{erf}\left(\frac{\ln\left(r_i + \frac{\Delta r}{2}\right) - \mu}{\sigma\sqrt{2}}\right)\,; \tag{B.6a}$$

$$P_i^- = \mathrm{erf}\left(\frac{\ln\left(r_i - \frac{\Delta r}{2}\right) - \mu}{\sigma\sqrt{2}}\right)\,. \tag{B.6b}$$